1D higher-order theories for quasi-static progressive failure analysis of composites based on a full 3D Hashin orthotropic damage model

Composites Part B 270 (2024) 111120

Contents lists available at ScienceDirect

Composites Part B

journal homepage: www.elsevier.com/locate/composites

1D higher-order theories for quasi-static progressive failure analysis of composites based on a full 3D Hashin orthotropic damage model

M. Trombini [a,1], M. Enea [a,1], M.R.T. Arruda [b,2], A. Pagani [a,3], M. Petrolo [a,*,3], E. Carrera [a,c,4]

[a] MUL² Lab, Department of Mechanical and Aerospace Engineering, Politecnico di Torino, 10129 Torino, Italy
[b] CERIS, Instituto Superior Técnico, Universidade de Lisboa, Lisboa, Portugal
[c] Department of Mechanical Engineering, College of Engineering, Prince Mohammad Bin Fahd University, Al Khobar, Kingdom of Saudi Arabia

ARTICLE INFO

Keywords:
Progressive failure
Carrera Unified Formulation
3D Hashin
Orthotropic damage model

ABSTRACT

This work investigates the crack propagation in composites by adopting a novel full three-dimensional (3D) Hashin-based orthotropic damage model combined with higher-order one-dimensional (1D) finite elements based on the Carrera Unified Formulation (CUF). Previous literature has proven that CUF provides structural formulations with great accuracy and improved computational efficiency. Moreover, a Layer-Wise (LW) formulation can be implemented within the CUF framework, allowing an accurate description of the 3D stress state in composite laminate, representing crucial information for progressive failure analysis. A Newton–Raphson predictor–corrector algorithm is used for the numerical solution of classical case tests, i.e., compact tension and three-point bending tests. The obtained results are compared with experimental outcomes and with solutions from well-established 2D damage models and a 3D Abaqus numerical model, demonstrating the capability of the proposed method to efficiently capture both the failure load and shape of the crack pattern.

1. Introduction

Composite materials are widely used in aerospace industries due to their specific properties. However, one of the major drawbacks in the analysis and design of composite structures is the accurate evaluation of the failure onset and progression within the structure to assess the influence of eventual damage on structural strength reduction. Furthermore, reliable failure theories and propagation methods are necessary to reduce the costs of the experimental campaigns, which are performed as predictive tools. Hence, an accurate methodology to complement extensive tests is a primary objective for aircraft companies.

The first step for a progressive failure analysis consists of the onset evaluation. There are currently various failure theories in the literature, such as the Tsai–Wu criterion [1], Hashin criterion [2], and those introduced by Puck and Schurmann [3,4], among others. The effectiveness of these failure criteria should be tested with a series of reliable experimental tests. Then, the following step is the correct reproduction of the failure progression. The selected methodology should show quantitative agreement with the experiments regarding the predicted initial and failure loads and qualitative agreement regarding the shape and size of damage zones. Moreover, the results should be independent of modeling features like mesh size.

Computational damage models for composite structures can be divided into two categories. The first category, based on discrete modeling, involves the explicit geometrical representation of cracks within the structure. This approach provides a physically realistic description of the damage mechanisms and their interactions but requires a significant computational effort. The discrete modeling approach typically makes use of interface elements, based on cohesive zone modeling, to simulate both matrix cracks within the ply and delamination between the plies [5–8]. Other discrete modeling techniques involve the eXtended-Finite Element Method (XFEM), where enriched kinematics are used to describe the displacement discontinuity across the crack [9]. An alternative to discrete modeling is the approach based on Continuum Damage Mechanics (CDM) [10], where the continuity of the displacement field in the finite element mesh is maintained. CDM techniques are popular due to their ease of implementation and relatively low computational cost. The individual cracks within the

* Correspondence to: MUL² Lab, Department of Mechanical and Aerospace Engineering, Politecnico di Torino, Corso Duca degli Abruzzi 24, 10129 Torino, Italy.
E-mail addresses: mattia.trombini@polito.it (M. Trombini), marco.enea@polito.it (M. Enea), mario.rui.arruda@tecnico.ulisboa.pt (M.R.T. Arruda), alfonso.pagani@polito.it (A. Pagani), marco.petrolo@polito.it (M. Petrolo), erasmo.carrera@polito.it (E. Carrera).
[1] PhD student.
[2] Research Associate.
[3] Associate Professor.
[4] Full Professor.

https://doi.org/10.1016/j.compositesb.2023.111120
Received 19 May 2023; Received in revised form 2 November 2023; Accepted 23 November 2023
Available online 29 November 2023

composite material are smeared out in CDM approaches and replaced with damage parameters in the constitutive relationship to describe the influence of such cracks on the global structural behavior. However, CDM methods generally show a strong mesh dependency, which can be reduced by scaling the fracture energy using a characteristic element length.

Early works that made use of CDM techniques are those introduced by Tan and co-workers [11–13], where three internal state variables are used to simulate the stiffness reduction of failed elements. This two-dimensional (2D) method is applied to composite laminates with central holes subjected to tensile or compressive in-plane loading conditions. In [14], the propagation of the damage in composite plates of a single-lap joint in tension is investigated. The material degradation rules are based on the Hashin failure criterion and are applied to each failed ply of the laminate. In [15], Basu et al. introduce a progressive failure method where each lamina degrades as characterized through laboratory experiments. This method also considers fiber microbuckling, which leads to the sudden degradation of the longitudinal lamina properties under compression loadings. Okabe et al. [16] present a work where a CDM method is applied to include transverse cracks in composite laminate modeling. In [17], Arruda et al. propose a novel 2D Tsai–Wu-based orthotropic damage model, which can identify the relevant failure methods within the Tsai–Wu framework.

A progressive failure analysis's accuracy also depends on the structural model adopted. Robbins and Reddy [18] demonstrated that classical lower-order structural theories, such as the first-order shear deformation theory, are unsuitable for progressive failure analysis in composite laminates. Thus, the necessity of higher-order or three-dimensional (3D) models arises. A first example is the work proposed by Camanho and Matthews [19]; here, a 3D FE model and a 3D failure criterion are adopted. Moreover, the authors consider a set of internal state variables which are a function of the type of damage and are used to degrade the material's elastic properties. A non-linear progressive damage model is introduced in [20], where Hashin and Matzenmiller–Lubliner–Taylor (MLT) failure criteria [21] are combined and applied to 3D woven composites. Huhne et al. [22] adopt a 3D Hashin failure criterion; however, this model does not consider any contribution from the interlaminar failure. Mandal and Chakrabarti propose one of the first examples of a fully 3D Hashin failure criterion in [23]. A recent example of the Hashin failure criterion for progressive failure analysis is proposed in [24], where the authors present a novel 3D orthotropic model with residual stresses. The algorithm is implemented in Abaqus through a user-made material subroutine, and it makes use of the viscous regularization [25] and secant matrix for the predictor–corrector algorithm.

The aforementioned 3D models can obtain accurate results if compared with experimental curves. Nevertheless, the computational cost of the analysis can increase considerably, making the resolution of complex problems almost prohibitive. For this reason, in the present work, the authors combine the Hashin-based 3D orthotropic model [24] with refined one-dimensional (1D) finite elements based on the Carrera Unified Formulation (CUF) [26]. The governing equations of CUF are written in terms of fundamental nuclei, which are invariant with the theory approximation order. The use of Lagrange polynomials for the expansion of the generalized displacements enables the implementation of a Layer-Wise (LW) formulation [27] within the CUF framework. LW provides displacement fields in every single layer and then imposes compatibility conditions at the interfaces between laminae, enabling the accurate reproduction of the complete 3D stress states in the laminate. The CUF capabilities have already been exploited for progressive failure analysis in concrete structures [28], and composite laminates [29,30], where a strain-based damage model, called CODAM2 [31,32], has been integrated within a CUF-based in-house code. The main novelties of the proposed framework stem from (i) the possibility of considering a damage model that takes into account a full 3D stress state for the evaluation of the failure onset and damage propagation, (ii) the inclusion of a simplified evolution of the shear damage, (iii) the computation of the 3D stress state via 1D CUF-based models for progressive failure problems, (iv) the use of a Newton–Raphson predictor–corrector algorithm in CUF for damage analysis. Results from the present formulation are validated on a single element and compared with experimental results from classical study cases, such as compact tension and three-point bending tests.

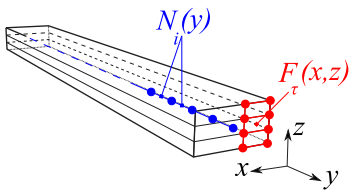

Fig. 1. Mathematical model for a one-dimensional beam within the CUF framework.

The paper is organized as follows: the fundamentals of the CUF formulation are introduced in Section 2, Section 3 presents the 3D Hashin formulation; then, the numerical results are illustrated in Section 4, and discussed in Section 5. Finally, the main conclusions are drawn in Section 6.

2. 1D CUF formulation

Let us consider a beam with the longitudinal axis aligned along the y-direction. The 3D displacement field in the CUF framework can be expressed as

$$\mathbf{u}(x, y, z) = F_\tau(x, z)\mathbf{u}_\tau(y), \qquad \tau = 1, 2, \dots, M \tag{1}$$

where $\mathbf{u}$ is the displacement vector, F_τ are the cross-section expansion functions; $\mathbf{u}_\tau$ is the generalized displacement vector; M is the number of terms in the expansion. Note that F_τ and M can be chosen arbitrarily, and their choice establishes the class of the adopted 1D CUF model. The present work employs Lagrange expansion (LE) models as cross-section functions. These models use Lagrange-like polynomials to expand the generalized displacement $\mathbf{u}_\tau$ over the beam section domain. The use of LE models allows to divide the cross-section into sub-regions, with a polynomial order depending on the Lagrange expansion adopted. Within the CUF framework, 4-node bilinear L4, 9-node biquadratic L9, and 16-node bicubic L16 models have been implemented. The isoparametric formulation is used to model arbitrarily shaped geometries. As an example, the displacement field for an L9 beam theory is given here:

$$\begin{aligned} u_x &= F_1\, u_{x_1} + F_2\, u_{x_2} + \cdots + F_9\, u_{x_9} \\ u_y &= F_1\, u_{y_1} + F_2\, u_{y_2} + \cdots + F_9\, u_{y_9} \\ u_z &= F_1\, u_{z_1} + F_2\, u_{z_2} + \cdots + F_9\, u_{z_9} \end{aligned} \tag{2}$$

where $u_{x_1}, \dots, u_{z_9}$ are the displacement variables of the problem, and they represent the translational displacement components of each of the nine nodes of the L9 polynomial. More information about the Lagrange element kinematics can be found in [33].

The main characteristic of LE models is that the displacement field is described by pure displacement variables placed over the cross-section domain. This feature permits to obtain 3D-like solutions at a global/local level and refining the model in limited regions of interest.

The generalized displacement $\mathbf{u}_\tau$ can be discretized by using 1D finite elements along the beam axis,

$$\boldsymbol{u}(x, y, z) = F_\tau(x, z)\, N_i(y)\, \boldsymbol{u}_{\tau i}, \quad \tau = 1, 2, \dots, M, \quad i = 1, 2, \dots, p+1 \tag{3}$$

where N_i are shape functions of order p and $\boldsymbol{u}_{\tau i}$ represents nodal displacement. A graphical representation of the mathematical model for a one-dimensional beam within the CUF framework is shown in Fig. 1.

The vector notation can be used to write both stress and strain tensors,

$$\boldsymbol{\sigma} = \{\sigma_{xx}\ \sigma_{yy}\ \sigma_{zz}\ \sigma_{xy}\ \sigma_{xz}\ \sigma_{yz}\}^T$$
$$\boldsymbol{\varepsilon} = \{\varepsilon_{xx}\ \varepsilon_{yy}\ \varepsilon_{zz}\ \varepsilon_{xy}\ \varepsilon_{xz}\ \varepsilon_{yz}\}^T \tag{4}$$

The strain–displacement relation is

$$\boldsymbol{\varepsilon} = \mathbf{B}\boldsymbol{u} \tag{5}$$

where $\mathbf{B}$ is the linear differential operator with two contributions,

$$\mathbf{B} = \mathbf{B}_\Omega + \mathbf{B}_y$$
$$\mathbf{B}_\Omega = \begin{bmatrix} \frac{\partial}{\partial x} & 0 & 0 \\ 0 & 0 & 0 \\ 0 & 0 & \frac{\partial}{\partial z} \\ 0 & \frac{\partial}{\partial x} & 0 \\ \frac{\partial}{\partial z} & 0 & \frac{\partial}{\partial x} \\ 0 & \frac{\partial}{\partial z} & 0 \end{bmatrix} \quad \mathbf{B}_y = \begin{bmatrix} 0 & 0 & 0 \\ 0 & \frac{\partial}{\partial y} & 0 \\ 0 & 0 & 0 \\ \frac{\partial}{\partial y} & 0 & 0 \\ 0 & 0 & 0 \\ 0 & 0 & \frac{\partial}{\partial y} \end{bmatrix} \tag{6}$$

The constitutive relation can be written as:

$$\boldsymbol{\sigma} = \mathbf{C}^{\mathrm{d}}\boldsymbol{\varepsilon} \tag{7}$$

where $\mathbf{C}^{\mathrm{d}}$ is the damage matrix. This work considers material nonlinearities due to damage, and a Newton–Raphson scheme is required to involve an iterative process. By using the principle of virtual work, the relation between the virtual variation of strain energy $(\delta L_{\mathrm{int}})$ and the work of external forces $(\delta L_{\mathrm{ext}})$ becomes:

$$\delta L_{\mathrm{int}} = \delta L_{\mathrm{ext}} \tag{8}$$

Considering V as the volume of the body, both the strain energy and the work of external forces can be derived by their integral formulation. Thus, the strain energy contribution reads:

$$\delta L_{\mathrm{int}} = \delta \boldsymbol{u}_{sj} \boldsymbol{k}_{\tau sij} \boldsymbol{u}_{\tau i} \tag{9}$$

where $\boldsymbol{k}_{\tau sij}$ is the Fundamental Nucleus (FN),

$$\boldsymbol{k}_{\tau sij} = \int_V \mathbf{B}_{sj}^T \mathbf{C}^{\mathrm{d}} \mathbf{B}_{\tau j}\, dV \tag{10}$$

The nucleus is a 3×3 matrix,

$$\boldsymbol{k}_{\tau sij} = \begin{bmatrix} k_{\tau sij}^{xx} & k_{\tau sij}^{xy} & k_{\tau sij}^{xz} \\ k_{\tau sij}^{yx} & k_{\tau sij}^{yy} & k_{\tau sij}^{yz} \\ k_{\tau sij}^{zx} & k_{\tau sij}^{zy} & k_{\tau sij}^{zz} \end{bmatrix} \tag{11}$$

For the sake of clarity, the $k_{\tau sij}^{xx}$ component is reported below:

$$\begin{aligned} k_{\tau sij}^{xx} = & \int_V C_{11}^d \frac{\partial}{\partial x}(N_j F_s) \frac{\partial}{\partial x}(N_i F_\tau) dV + \int_V C_{16}^d \frac{\partial}{\partial x}(N_j F_s) \frac{\partial}{\partial y}(N_i F_\tau) dV \\ & + \int_V C_{44}^d \frac{\partial}{\partial z}(N_j F_s) \frac{\partial}{\partial z}(N_i F_\tau) dV + \int_V C_{16}^d \frac{\partial}{\partial y}(N_j F_s) \frac{\partial}{\partial x}(N_i F_\tau) dV \\ & + \int_V C_{66}^d \frac{\partial}{\partial y}(N_j F_s) \frac{\partial}{\partial y}(N_i F_\tau) dV \end{aligned} \tag{12}$$

Similarly, the compact notation for the external force energy is

$$\delta L_{\mathrm{ext}} = \delta \boldsymbol{u}_{sj} \boldsymbol{p}_{sj} \tag{13}$$

$\boldsymbol{p}_{sj}$ is the external load vector. By iterating indices, τ, s, i, j, the global stiffness matrix (see Fig. 2), and global load vector are built. Further information about the matrix generation can be found in [26]. Concerning the iteration strategy for the nonlinear solution process, the equilibrium equation is given by:

$$\boldsymbol{F}_{int}(\boldsymbol{u}) - \boldsymbol{F}_{ext} = 0 \tag{14}$$

where $\boldsymbol{F}_{int}(\boldsymbol{u})$ is the internal force vector that depends on the displacement vector, and $\boldsymbol{F}_{ext}$ is the external force vector. The Newton–Raphson

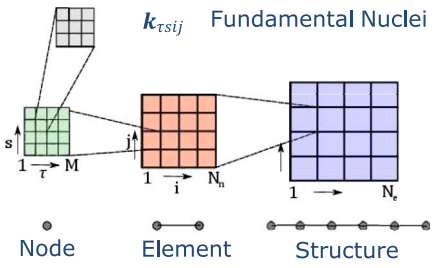

Fig. 2. Stiffness matrix assembly in CUF.

scheme involves the parametrization of the external load by a factor λ_n at a pseudo-time instant t_n. Consequently, Eq. (14) holds as follows:

$$\boldsymbol{F}_{int}(\boldsymbol{u}) - \lambda_n \boldsymbol{F}_{ext} = 0 \tag{15}$$

The implicit integration scheme uses an iterative process to find the converged solution $\boldsymbol{u}_{n+1}$, starting from the known solution $\boldsymbol{u}_n$. Considering the Taylor series expansion truncated at the linear term [34], the internal force $\boldsymbol{F}_{int}(\boldsymbol{u}_{n+1})$ states:

$$\boldsymbol{F}_{int}\left(\boldsymbol{u}_{n+1}^{k+1}\right) = \boldsymbol{F}_{int}\left(\boldsymbol{u}_{n+1}^{k}\right) + \frac{\partial \boldsymbol{F}_{int}\left(\boldsymbol{u}_{n+1}^{k}\right)}{\partial \boldsymbol{u}_{n+1}^{k}} \Delta\boldsymbol{u}, \quad \Delta\boldsymbol{u} = \left(\boldsymbol{u}_{n+1}^{k+1} - \boldsymbol{u}_{n+1}^{k}\right) \tag{16}$$

where k is the iteration index for the load increment $[n, n+1]$, and Δu is the incremental displacement. Consequently, the tangent stiffness matrix $\boldsymbol{K}^T$ can be defined as follows:

$$\boldsymbol{K}^T = \frac{\partial \boldsymbol{F}_{int}\left(\boldsymbol{u}_{n+1}^{k}\right)}{\partial \boldsymbol{u}_{n+1}^{k}} \tag{17}$$

In CUF, $\boldsymbol{K}^T$ reads:

$$\boldsymbol{k}_{\tau sij}^T \Delta\boldsymbol{u}_{\tau i} = \boldsymbol{\phi}_{sj} \tag{18}$$

with $\boldsymbol{k}_{\tau sij}^T$ as FN of the tangent stiffness matrix and $\boldsymbol{\phi}_{sj}$ as FN of the residual force vector. The displacement-based convergence criterion can be identified as follows:

$$\frac{\|\Delta\boldsymbol{u}_{n+1}^{k}\|}{\|\boldsymbol{u}_{n+1}\|} \leq \text{tolerance} \tag{19}$$

3. 3D Hashin damage model framework

This section describes the orthotropic damage model used in the current work. First, the constitutive relation for a damaged material is shown, including the definition of the damage variables. Then, the failure initiations are introduced in terms of failure criteria. Finally, the linear damage evolution law describing the failure progression of the independent crack modes is illustrated.

3.1. Stiffness formulation

The current orthotropic model deals with the assembly of the secant stiffness matrix in the damaged state $\mathbf{C}^{\mathrm{d}}$, used to compute the constitutive elastic stress–strain relation. By inverting the compliance matrix $\mathbf{S}^{\mathrm{d}}$ (Eq. (20)), the stiffness matrix $\mathbf{C}^{\mathrm{d}}$ is later computed.

$$\mathbf{S}^{\mathrm{d}} = \begin{bmatrix} \frac{S_{11}}{1-d_f} & S_{12} & S_{13} & 0 & 0 & 0 \\ S_{21} & \frac{S_{22}}{1-d_m} & S_{23} & 0 & 0 & 0 \\ S_{31} & S_{32} & \frac{S_{33}}{1-d_i} & 0 & 0 & 0 \\ 0 & 0 & 0 & \frac{S_{44}}{1-ds_{12}} & 0 & 0 \\ 0 & 0 & 0 & 0 & \frac{S_{55}}{1-ds_{13}} & 0 \\ 0 & 0 & 0 & 0 & 0 & \frac{S_{66}}{1-ds_{23}} \end{bmatrix} \tag{20}$$

With

$$S_{jj} = \frac{1}{E_{jj}}, \quad S_{jk} = S_{kj} = \frac{\nu_{jk}}{E_{jj}} = \frac{\nu_{kj}}{E_{kk}}, \quad j,k = 1,2,3, \quad j \neq k$$
$$S_{44} = G_{12}, \quad S_{55} = G_{13}, \quad S_{66} = G_{23} \tag{21}$$

The compliance matrix, assembled with the damage terms along the main diagonal, guarantees the consistency of the model and the thermodynamic admissibility [21,32,35]. The damage variables d_f, d_m, d_i refer to the fiber, matrix, and interlaminar failure modes, respectively, and both tensile and compressive behavior are activated using the relative effective stress $\hat{\sigma}_j$ [36]:

$$\hat{\sigma}_j = \frac{\sigma_j}{1 - d_j}, \qquad j = 1,2,\dots,6 \tag{22}$$

With

$$d_f = d_1 = \begin{cases} d_{ft} & \text{if } \hat{\sigma}_1 \geq 0 \\ d_{fc} & \text{if } \hat{\sigma}_1 \leq 0 \end{cases}$$
$$d_m = d_2 = \begin{cases} d_{mt} & \text{if } \hat{\sigma}_2 \geq 0 \\ d_{mc} & \text{if } \hat{\sigma}_2 \leq 0 \end{cases} \tag{23}$$
$$d_i = d_3 = \begin{cases} d_{it} & \text{if } \hat{\sigma}_3 \geq 0 \\ d_{ic} & \text{if } \hat{\sigma}_3 \leq 0 \end{cases}$$

The terms ds_{12}, ds_{13} and ds_{23} regulate the shear damage evolution, which depends on the fiber, matrix, and interlaminar damages, as stated in the following equation:

$$\begin{cases} ds_{12} = d_4 = 1 - (1 - d_{ft})(1 - d_{fc})(1 - d_{mt})(1 - d_{mc}) \\ ds_{13} = d_5 = 1 - (1 - d_{ft})(1 - d_{fc})(1 - d_{it})(1 - d_{ic}) \\ ds_{23} = d_6 = 1 - (1 - d_{mt})(1 - d_{mc})(1 - d_{it})(1 - d_{ic}) \end{cases} \tag{24}$$

The detailed stiffness formulation and the demonstration of thermodynamic consistency are available in [17,24].

3.2. Failure onset and damage evolution

The onset of damage depends on the current stress field over the material. The damages involved in this framework include both tensile and compressive failure modes, and the simplifications adopted for the proposed model are described in [2,24]. The fiber damage initiation in the longitudinal direction occurs when the failure criterion $F_f = 1$, where:

$$F_f = \begin{cases} F_{ft} = \left(\frac{\hat{\sigma}_1}{X_t}\right)^2 + \frac{\hat{\tau}_{12}^2 + \hat{\tau}_{13}^2}{S_L^2}, & \text{if } \hat{\sigma}_1 \geq 0 \\ F_{fc} = \left(\frac{\hat{\sigma}_1}{X_c}\right)^2, & \text{if } \hat{\sigma}_1 < 0 \end{cases} \tag{25}$$

X_t and X_c represent the fiber tensile and compressive strengths, whereas S_L is the longitudinal shear strength. In the same manner, matrix F_m and interlaminar F_i failure criteria are defined,

$$F_m = \begin{cases} F_{mt} = \left(\frac{\hat{\sigma}_2 + \hat{\sigma}_3}{Y_t}\right)^2 + \frac{\hat{\tau}_{23}^2 - \hat{\sigma}_2\hat{\sigma}_3}{S_I^2} + \frac{\hat{\tau}_{21}^2 + \hat{\tau}_{31}^2}{S_L^2}, & \text{if } \hat{\sigma}_2 + \hat{\sigma}_3 \geq 0 \\ F_{mc} = \left[\left(\frac{Y_c}{2S_T}\right)^2 - 1\right]\left(\frac{\hat{\sigma}_2 + \hat{\sigma}_3}{Y_c}\right) + \left(\frac{\hat{\sigma}_2 + \hat{\sigma}_3}{2S_T}\right)^2 & \\ \quad + \frac{\hat{\tau}_{23}^2 - \hat{\sigma}_2\hat{\sigma}_3}{S_I^2} + \frac{\hat{\tau}_{21}^2 + \hat{\tau}_{31}^2}{S_L^2}, & \text{if } \hat{\sigma}_2 + \hat{\sigma}_3 < 0 \end{cases} \tag{26}$$

$$F_i = \begin{cases} F_{it} = \left(\frac{\hat{\sigma}_3}{Z_t}\right)^2 + \left(\frac{\hat{\tau}_{31}}{S_L}\right)^2 + \left(\frac{\hat{\tau}_{31}}{S_I}\right)^2, & \text{if } \hat{\sigma}_3 \geq 0 \\ F_{ic} = \left(\frac{\hat{\sigma}_3}{Z_c}\right)^2, & \text{if } \hat{\sigma}_3 < 0 \end{cases} \tag{27}$$

Y_t and Y_c are the matrix tensile and compressive strengths, Z_t and Z_c are the interlaminar tensile and compressive strengths, whereas S_T and S_I indicate the transversal and interlaminar shear strengths. According to [24], the computation of equivalent stress and strain is as follows:

$$\sigma_{eq}\varepsilon_{eq} = \sum \sigma_{ij}\varepsilon_{ij}, \quad \text{with} \quad \varepsilon_{eq} = \sqrt{\sum \varepsilon_{ij}^2}, \qquad i,j = 1,2,\dots,6 \tag{28}$$

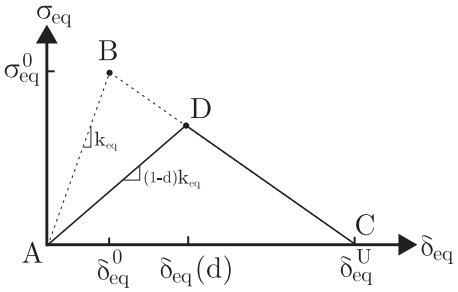

Fig. 3. Constitutive relation for the equivalent stress and displacement.

ε_{eq} and σ_{eq} are the equivalent strain and stress consistent with [37],

$$\begin{cases} \varepsilon_{eq,ft} = \sqrt{\langle\varepsilon_1\rangle^2 + \gamma_{12}^2 + \gamma_{13}^2} \\ \varepsilon_{eq,fc} = \langle -\varepsilon_1 \rangle \\ \varepsilon_{eq,mt} = \sqrt{\langle\varepsilon_2\rangle^2 + \langle\varepsilon_3\rangle^2 + \gamma_{21}^2 + \gamma_{23}^2 + \gamma_{31}^2} \\ \varepsilon_{eq,mc} = \sqrt{\langle -\varepsilon_2\rangle^2 + \langle -\varepsilon_3\rangle^2 + \gamma_{21}^2 + \gamma_{23}^2 + \gamma_{31}^2} \\ \varepsilon_{eq,it} = \sqrt{\langle\varepsilon_3\rangle^2 + \gamma_{31}^2 + \gamma_{32}^2} \\ \varepsilon_{eq,ic} = \langle -\varepsilon_3 \rangle \end{cases} \tag{29}$$

$$\begin{cases} \sigma_{eq,ft} = \frac{\langle\sigma_1\rangle\langle\varepsilon_1\rangle + \tau_{12}\gamma_{12} + \tau_{13}\gamma_{13}}{\sqrt{\langle\varepsilon_1\rangle^2 + \gamma_{12}^2 + \gamma_{13}^2}} \\ \sigma_{eq,fc} = \langle -\sigma_1 \rangle \\ \sigma_{eq,mt} = \frac{\langle\sigma_2\rangle\langle\varepsilon_2\rangle + \langle\sigma_3\rangle\langle\varepsilon_3\rangle + \tau_{21}\gamma_{21} + \tau_{23}\gamma_{23} + \tau_{31}\gamma_{31}}{\sqrt{\langle\varepsilon_2\rangle^2 + \langle\varepsilon_3\rangle^2 + \gamma_{21}^2 + \gamma_{23}^2 + \gamma_{31}^2}} \\ \sigma_{eq,mc} = \frac{\langle -\sigma_2\rangle\langle -\varepsilon_2\rangle + \langle -\sigma_3\rangle\langle -\varepsilon_3\rangle + \tau_{21}\gamma_{21} + \tau_{23}\gamma_{23} + \tau_{31}\gamma_{31}}{\sqrt{\langle -\varepsilon_2\rangle^2 + \langle -\varepsilon_3\rangle^2 + \gamma_{21}^2 + \gamma_{23}^2 + \gamma_{31}^2}} \\ \sigma_{eq,it} = \frac{\langle\sigma_3\rangle\langle\varepsilon_3\rangle + \tau_{31}\gamma_{31} + \tau_{32}\gamma_{32}}{\sqrt{\langle\varepsilon_3\rangle^2 + \gamma_{31}^2 + \gamma_{32}^2}} \\ \sigma_{eq,ic} = \langle -\sigma_3 \rangle \end{cases} \tag{30}$$

where $\langle\cdot\rangle$ denotes the Macaulay bracket. By solving the failure criteria defined in Eqs. (25), (26), and (27), the initial equivalent stress σ_{eq}^0 and strain ε_{eq}^0 are then retrieved. The calculation of equivalent stress and strain in the onset of damage is required to define the constitutive evolution law. In this work, the damage evolution follows a linear softening path, and the damage d in the post-peak branch is defined using the following equation:

$$d = \begin{cases} \frac{\delta_{eq}^u\left(\delta_{eq} - \delta_{eq}^0\right)}{\delta_{eq}\left(\delta_{eq}^u - \delta_{eq}^0\right)}, & \text{if } \delta_{eq}^0 \leq \delta_{eq} \leq \delta_{eq}^u \\ 1, & \text{if } \delta_{eq} > \delta_{eq}^u \end{cases} \tag{31}$$

where δ_{eq} is the equivalent displacement, and δ_{eq}^u is considered as the equivalent displacement when the damage $d = 1$.

$$\delta_{eq} = L_c\varepsilon_{eq} \quad \text{and} \quad \delta_{eq}^u = \frac{2G_a}{\sigma_{eq}} \tag{32}$$

L_c stands for the characteristic length [38], used to reduce the mesh dependency. The current work considers $L_c = (VGP)^{\frac{1}{3}}$, where VGP is the Gauss point volume of the given element, as previously done in [29]. However, different approaches can be exploited to define the characteristic length, as shown in [39]. G_a represents the fracture energy of the independent damage mode a, corresponding to the area $A\hat{B}C \Rightarrow \left(\varepsilon_{eq}(d=0)\right)$ under the curve of the linear evolution law (see Fig. 3).

4. Numerical results

This section provides the numerical verification and validation of the Hashin damage model within the CUF framework, comparing the

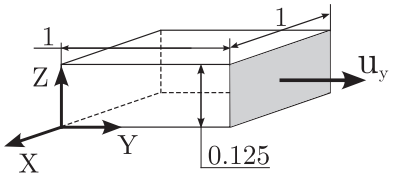

Fig. 4. Geometry and dimensions in mm of the single element.

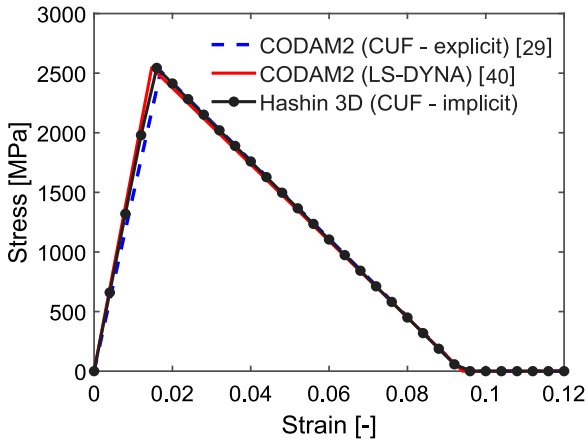

Fig. 5. Stress–strain of the single element under uniaxial longitudinal load.

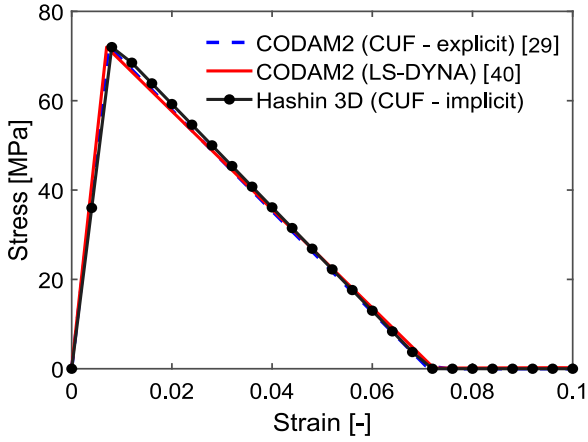

Fig. 6. Stress–strain of the single element under uniaxial transversal load.

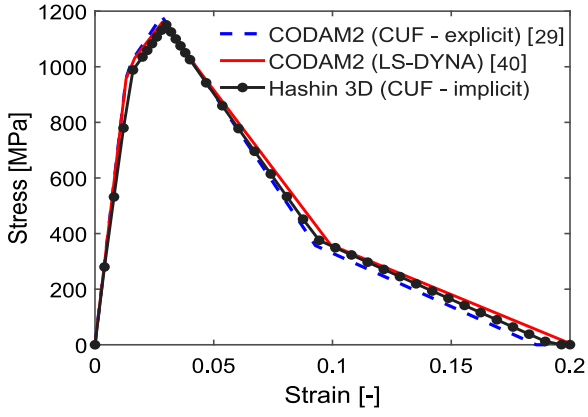

Fig. 7. Stress–strain of the single element with a ply sequence of $[90/45/0\text{-}45]_{2s}$ under uniaxial load.

outcomes with the results of well-established 2D damage models. Then, the current framework is used to predict the damage evolution of two assessments with experimental results and 3D Abaqus numerical analyses.

4.1. Single element verification

This section presents the verification of the damage model. The architecture consists of a single element under a uniaxial load. The discretization consists of a 2-node linear finite element (B2) along the y-direction and a single L4 for the cross-section. The material is IM7/8552 carbon fiber reinforced polymer (CFRP), and the properties are listed in Table 1, according to [29]. Tables 2 and 3 contain the strength of the material and its fracture energies. The interlaminar properties are assumed to be the same as the matrix properties. The representation of the single element used to validate the implementation of the damage model can be observed in Fig. 4.

The first numerical assessment consists of a longitudinal tension leading to the failure of fibers along the y-direction. Fig. 5 shows the stress–strain curve for this case, comparing the current 3D damage model within a CUF framework with the second-generation COmposite DAMage (CODAM2), which has been implemented by using CUF [29] and LS-DYNA [40]. The tensile matrix failure mode is also explored by applying tension along the y-direction and setting the fibers in the x-direction. The relative stress–strain curve is illustrated in Fig. 6. The last numerical test involves a quasi-isotropic laminate with a ply sequence of $[90/45/0\text{-}45]_{2s}$ under uniaxial load. A B2 element acts along the y-direction, and an L4 element for each ply is involved. Fig. 7 shows the stress–strain curve for the quasi-isotropic case, while Fig. 8 compares the evolution of damage in some layers with the work of Reiner et al. [40].

Based on the results, the following comments can be raised:

1. The implementation of the Hashin damage model within a 1D CUF framework generates results consistent with the references, and the peak stresses coincide with longitudinal and transverse strengths.
2. The damage model manages to handle different laminations, and the results are in good agreement with the reference, as illustrated in Fig. 7. Minor inconsistencies with the CODAM2 can be detected in the softening path; however, the peak force and the displacement at the peak are consistent.

4.2. Compact tension test

This assessment concerns the damage analysis of a pultruded glass fiber reinforced polymer (GFRP) compact tension (CT) specimen. The material properties are listed in Table 4, derived from the work of [41, 42]. The specimen thickness is equal to 10 mm [41]. The data concerning the strengths and fracture energies of the pultruded GFRP are in Tables 5 and 6. The fibers are set along the z-direction, while the in-plane transversal direction is along the x-direction. The lower pin is clamped, and the vertical displacement in the upper pin gradually increases from 0 to the final displacement. The discretization consists of L4 and L9 for the cross-section, and the numerical case also involves a convergence analysis on the order of the adopted beam element, i.e., 2-node linear (B2), 3-node quadratic (B3) and 4-node cubic (B4) finite elements involving different configurations. The details about the geometry and an example of the adopted cross-section discretization can be found in Fig. 9.

Fig. 10 shows the force–displacement curves for the CUF results, comparing the outcomes with both the experimental campaign [43] and 3D Abaqus curve [24], where 8-node brick solid finite elements (C3D8) are employed. Fig. 10(a) illustrates the convergence analysis on the number of elements over the cross-section. Fig. 10(b) focuses on the effect of both mesh size and order of discretization, and specifically,

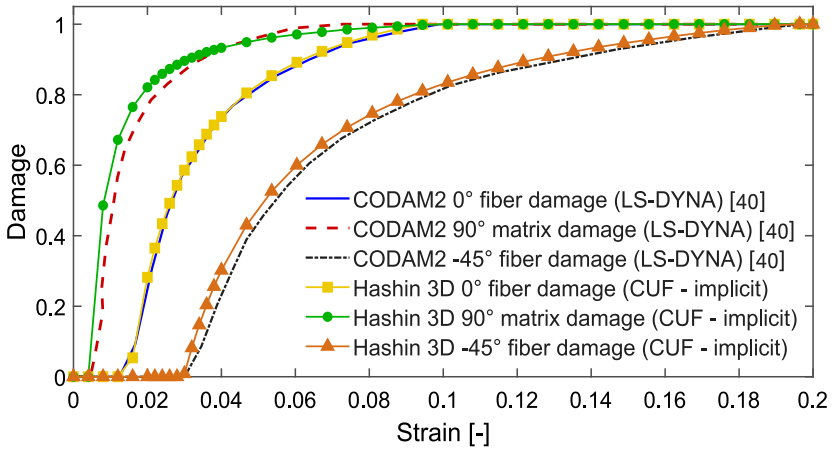

Fig. 8. Comparison of CUF fiber and matrix damage evolutions with CODAM2 framework for the quasi-isotropic single element.

Table 1
Material properties of IM7/8552 carbon fiber reinforced polymer.

E_{11} [GPa]	E_{22} [GPa]	E_{33} [GPa]	G_{12} [GPa]	G_{13} [GPa]	G_{23} [GPa]	ν_{12} [-]	ν_{13} [-]	ν_{23} [-]
165.00	9.00	9.00	5.60	5.60	2.80	0.34	0.34	0.5

Table 2
Longitudinal, transverse, interlaminar and shear strength of CFRP for the single element.

X_T [MPa]	X_C [MPa]	Y_T [MPa]	Y_C [MPa]	Z_T [MPa]	Z_C [MPa]	S_L [MPa]	S_T [MPa]	S_I [MPa]
2560.00	1690.00	73.00	250.00	73.00	250.00	90.00	90.00	90.00

Table 3
Fracture energies of CFRP for the single element.

G_{ft} [MPa·mm]	G_{fc} [MPa·mm]	G_{mt} [MPa·mm]	G_{mc} [MPa·mm]	G_{it} [MPa·mm]	G_{ic} [MPa·mm]
120.00	80.00	2.60	4.20	2.60	4.20

Table 4
Material properties of the GFRP material for the CT test in the material reference system.

E_{11} [GPa]	E_{22} [GPa]	E_{33} [GPa]	G_{12} [GPa]	G_{13} [GPa]	G_{23} [GPa]	ν_{12} [-]	ν_{13} [-]	ν_{23} [-]
30.00	12.00	12.00	3.00	3.00	2.50	0.24	0.24	0.30

Table 5
Longitudinal, transverse, interlaminar and shear strength of the GFRP material for the CT test.

X_T [MPa]	X_C [MPa]	Y_T [MPa]	Y_C [MPa]	Z_T [MPa]	Z_C [MPa]	S_L [MPa]	S_T [MPa]	S_I [MPa]
323.00	426.00	71.00	71.00	71.00	71.00	67.00	64.00	64.00

the difference between lower and higher-order kinematic theories in the load–displacement curve is investigated. Table 7 compares the CUF maximum reaction and vertical displacement at peak with both experimental and 3D Abaqus outcomes, and the number of degrees of freedom (DOF) for the numerical tests is listed. Fig. 11 shows the evolution of the tensile matrix damage in the narrow band of the specimen for different applied vertical displacements. Moreover, according to [17], the current damage framework manages to recognize an evolution of the compressive matrix damage in the specimen as illustrated in Fig. 12, whereas Fig. 13 displays the final shear damage distributions.

In continuum damage mechanics, the inherent mesh sensitivity associated with the choice of elements can be a significant issue [44]. According to [45], mesh sensitivity arises when altering the type or distortion of finite elements within a fixed mesh, potentially leading to variations in the solution depending on the selected type or distortion of finite elements. In 1D CUF, the sensitivity should be assessed by considering (i) the finite element mesh along the y-direction, involving linear, quadratic, and cubic finite elements, namely, 2-node B2, 3-node B3, and 4-node B4; (ii) across the cross-section, where the choice is between 4-node bilinear L4 expansions and 9-node biquadratic L9 expansions. Consequently, in CUF, the mesh sensitivity relates to the impact of FEM elements acting along the y-direction, whereas a structural theory sensitivity can be proposed for the cross-section. Focusing on the narrow band where the damage is located, three different sets of expansions — 7, 8, and 9 elements — are employed along the z-direction, and the width of each element is shown in Fig. 14. Fig. 15(a) shows the variation in the peak load using 4-node bilinear elements for the cross-section when the number of beam elements increases, and accordingly, the width decreases; the same histogram is shown in Fig. 15(b) with 9-node biquadratic elements for the cross-section.

The sensitivity of the structural theory is further investigated by varying the order of the elements over the cross-section while fixing both the size of the elements in the narrow band and the FEM discretization. Table 8 reports the predicted peak load, whereas Table 9 includes the percentage deviation between the structural theories for each FEM discretization. Considering the biquadratic L9 as structural theory, the influence of mesh size in the narrow band can be analyzed. The decreasing trend of the percentage variation is shown in Fig. 16, while the order of FEM discretization increases.

Table 6
Fracture energies of the pultruded GFRP for the CT test.

G_{ft} [MPa·mm]	G_{fc} [MPa·mm]	G_{mt} [MPa·mm]	G_{mc} [MPa·mm]	G_{it} [MPa·mm]	G_{ic} [MPa·mm]
100.00	100.00	20.00	20.00	20.00	20.00

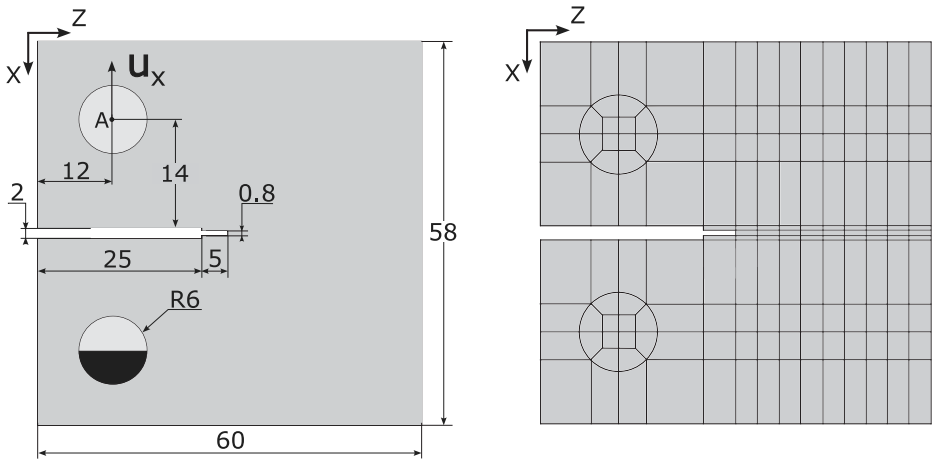

Fig. 9. Dimensions in mm of the specimen for the CT test and an example of the cross-section discretization using biquadratic L9 elements.

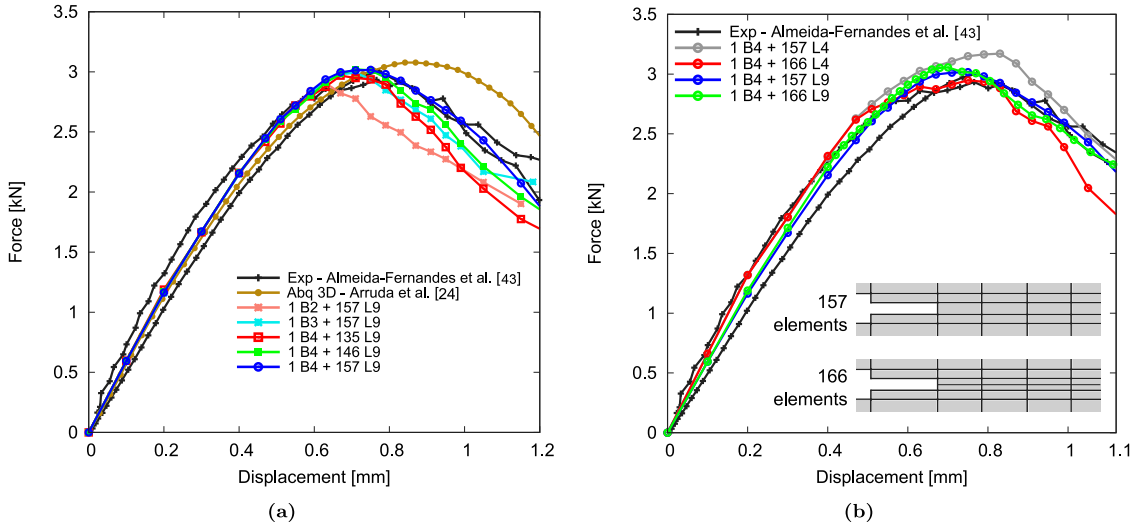

Fig. 10. Vertical load–displacement convergence analysis in the cross-section (a) and in the narrow band (b) for the CT test. The cross-section discretizations in the notch are also shown.

Table 7
Comparison of CUF maximum reaction and vertical displacement with experimental and 3D Abaqus results, and DOF of each model for the CT test.

Case	Total DOF	Peak load [kN]	Vertical displacement at peak [mm]
Reference solutions			
Exp 1 — Almeida-Fernandes et al. [43]	–	2.933	0.763
Exp 2 — Almeida-Fernandes et al. [43]	–	3.009	0.776
3D Abaqus — Arruda et al.[24]	66900[a]	3.075	0.834
Present 1D CUF models			
1D CUF 1 B2 + 157 L9	4818[b]	2.906	0.629
1D CUF 1 B3 + 157 L9	6885[b]	3.000	0.689
1D CUF 1 B4 + 135 L9	7848[b]	3.022	0.710
1D CUF 1 B4 + 146 L9	8400[b]	3.025	0.730
1D CUF 1 B4 + 157 L9	8952[b]	3.025	0.730
1D CUF 1 B4 + 157 L4	3420[b]	3.179	0.810
1D CUF 1 B4 + 166 L4	3540[b]	2.959	0.770
1D CUF 1 B4 + 166 L9	9408[b]	3.056	0.700

[a] Symmetric along *y*-direction.
[b] Full structure.

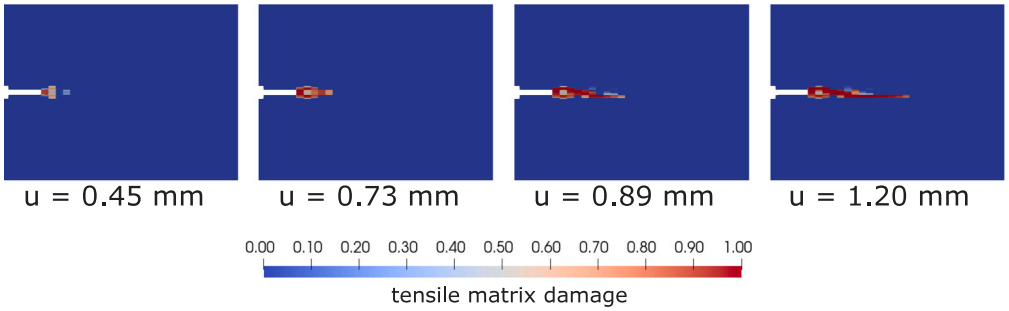

Fig. 11. Evolution of tensile matrix damage in the narrow band for the case with 1 B4 + 157 L9 of the CT test.

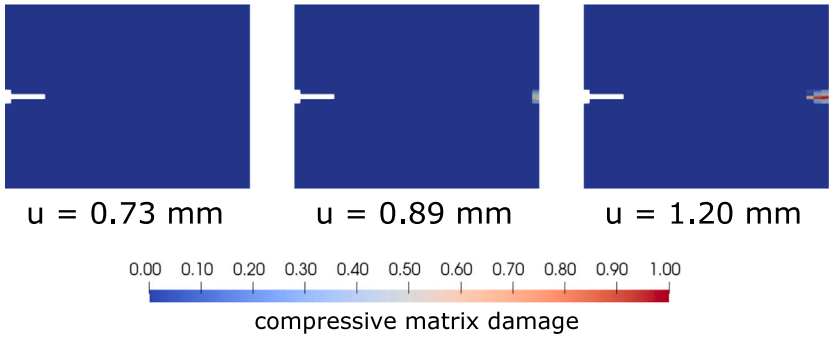

Fig. 12. Evolution of compressive matrix damage in the narrow band for the case with 1 B4 + 157 L9 of the CT test.

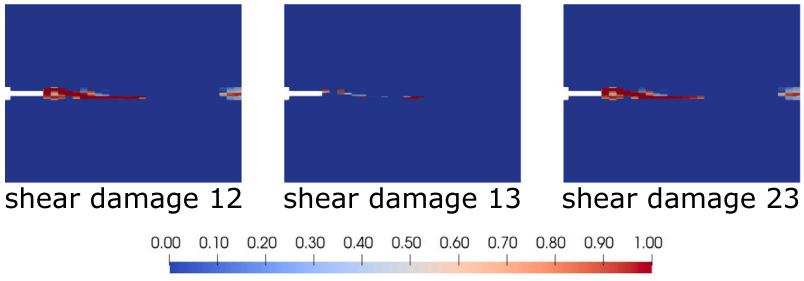

Fig. 13. Final distribution of the shear damage in the narrow band for the case with 1 B4 + 157 L9 of the CT test.

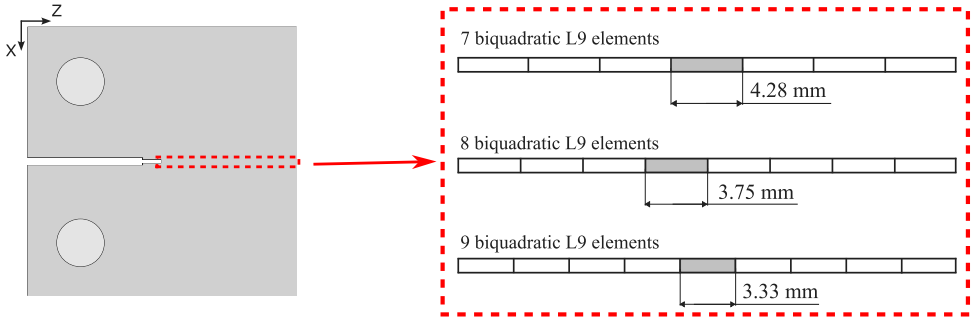

Fig. 14. Number of expansion elements in the narrow band for the CT coupon, including the width of a single element.

By observing the results and assuming the case of 1 B4 + 157 L9 as CUF reference, some considerations are made:

1. The convergence analysis demonstrates that using cubic elements for the thickness leads to a good agreement with the experimental curves, also considering a coarser cross-section discretization. The CUF framework is also highly cost-effective compared to 3D Abaqus, thus maintaining a significant accuracy in the peak detection and the softening path.
2. From Fig. 10(a), CUF results can predict the softening branch behavior in a better agreement with the experimental campaign than the 3D Abaqus. The current work involves an approach based on the cubic root of the Gauss point volume associated with a given element. In contrast, the square root of the numerically calculated surface area was adopted in [24]. In addition, the current order of the kinematic theories is higher than the Abaqus framework.

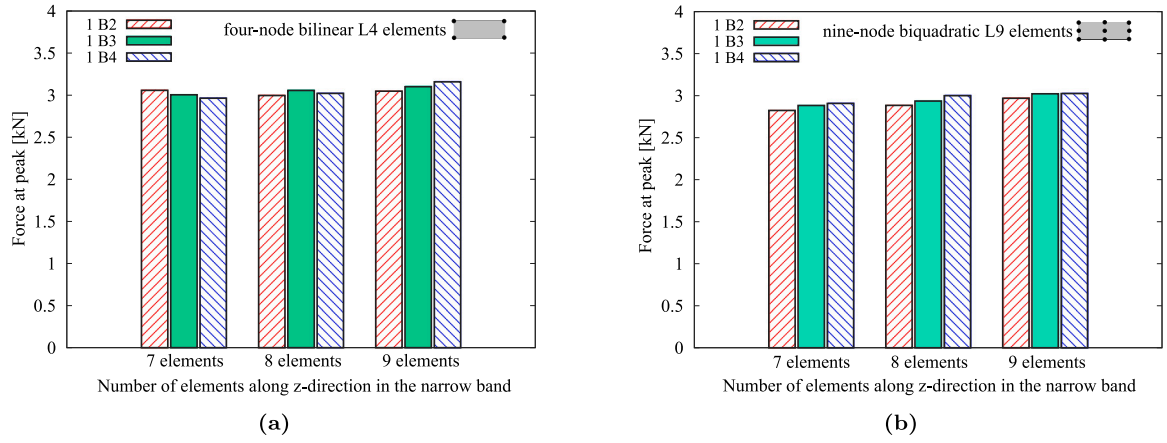

Fig. 15. FEM mesh and structural theory sensitivity when the cross-section of the CT has (a) 4-node L4 elements and (b) 9-node L9 elements.

Table 8
Predicted peak load for each element mesh size in the narrow band by varying the structural theory and the type of FEM element for the CT test.

Structural theory	FEM element	Peak load [kN]		
		7 elements	8 elements	9 elements
Bilinear L4	B2	3.057	3.005	2.964
	B3	2.996	3.056	3.021
	B4	3.097	3.161	3.179
Biquadratic L9	B2	2.824	2.883	2.907
	B3	2.884	2.936	3.000
	B4	2.969	3.022	3.025

Table 9
Percentage variation between the peaks with L4 and L9 for different element sizes in the narrow section, varying the order of the FEM element along the y-direction.

FEM element	Percentage variation		
	7 elements	8 elements	9 elements
B2	7.9%	4.1%	1.9%
B3	3.8%	4.0%	0.7%
B4	4.2%	4.5%	4.9%

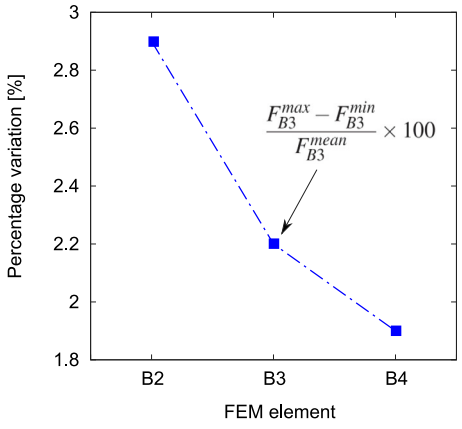

Fig. 16. Percentage variation of peak load for L9 structural theory with different FEM elements.

3. By comparing the maximum reaction in Table 7, reference CUF maximum force results 1.82% higher than mean experimental values, resulting more accurate than 3D Abaqus, which generates a larger outcome. On the other hand, regarding the vertical displacement at peak, the CUF outcome is 2.5% smaller than mean experimental displacements. In addition, the number of DOF used within the CUF framework is significantly less than [24], resulting in a decrease in the computational cost.
4. The distribution of shear damage demonstrates that both fiber and interlaminar damages occur, even though their value is negligible compared to matrix damage evolution. To conclude, the 3D damage model can detect the damage evolution in the transversal out-of-plane y-direction, thus including an effect that prior 2D damage models did not manage to consider.
5. The sensitivity analysis demonstrates that slight differences in the peak detection can be obtained when using a quadratic or cubic FEM element along the y-direction, with a biquadratic discretization of the cross-section, as depicted in Fig. 15(b).
6. The structural theory sensitivity highlighted that a minor sensitivity is present when using 4-node B4 elements as FEM discretization but remains almost constant with different mesh sizes in the narrow band. For the cases with B2 and B3, the smallest size of the narrow section elements leads to a significant decrease in the structural theory sensitivity, see Table 9. However, Fig. 16 shows that employing higher-order elements leads to a significant reduction of the mesh-size dependency for the prediction of peak load.

4.3. Three-point bending beam

This case aims to provide the damage evolution in a three-point bending GFRP beam with a notch at the midspan. To reduce the cost of the analysis, the numerical simulation considers only a quarter of the beam, and the relative geometry is in Fig. 17. FE models with B2, B3, and B4 finite elements act along the y-direction of the beam, whereas the cross-section discretization consists of biquadratic L9 expansion elements as shown in Fig. 18. Table 10 lists the adopted material properties, based on [17,24], with fibers set along the x-direction, and Tables 11 and 12 contain the damage properties. The beam is simply-supported, and a steel support applies a vertical displacement, as previously done in [24].

Five analysis cases are considered using different discretizations for both axial and cross-sectional domains. Table 13 specifies the number of FEM elements and the relative discretization for section A–A (see Fig. 18). Fig. 19 plots vertical reaction-crack mouth opening displacement (CMOD) curves of CUF results, an Abaqus 3D employing C3D8 elements [24], and an experimental campaign [46]. Moreover, a detailed comparison of maximum reaction force, CMOD, and numerical DOF is presented in Table 14. Finally, Fig. 20 shows the evolution of the tensile matrix damage during the analysis, and the ultimate distribution of some representative damage modes is illustrated in Fig. 21.

Assuming case C as the CUF reference, the results suggest that:

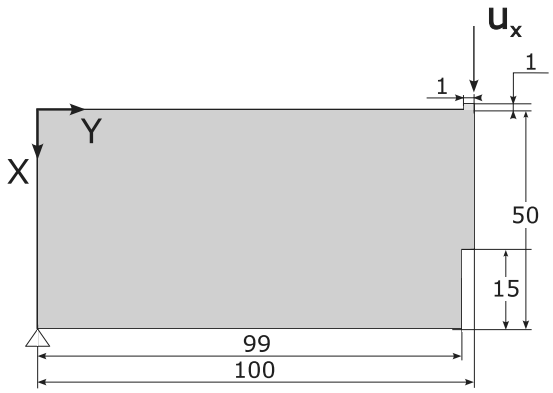

Fig. 17. Dimensions in mm of the specimen for the three-point bending beam and applied boundary conditions.

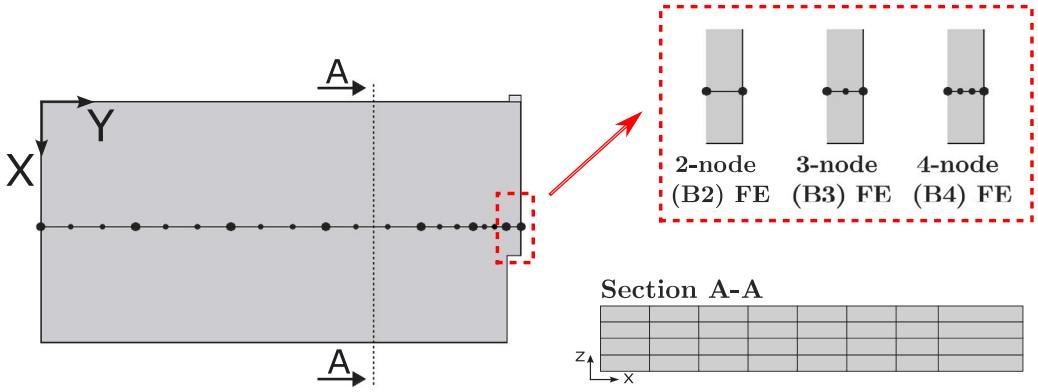

Fig. 18. Finite element discretization along the y-direction for the three-point bending beam with a magnification in the narrow section and an example of an in-plane discretization for the section A–A.

Table 10
Material properties of the GFRP material for the three-point bending beam and steel support in the material reference system.

E_{11} [GPa]	E_{22} [GPa]	E_{33} [GPa]	G_{12} [GPa]	G_{13} [GPa]	G_{23} [GPa]	ν_{12} [-]	ν_{13} [-]	ν_{23} [-]
30.00	11.38	11.38	3.00	3.00	3.00	0.24	0.24	0.4

Table 11
Longitudinal, transverse, interlaminar and shear strength of the GFRP material for the three-point bending beam.

X_T [MPa]	X_C [MPa]	Y_T [MPa]	Y_C [MPa]	Z_T [MPa]	Z_C [MPa]	S_L [MPa]	S_T [MPa]	S_I [MPa]
323.00	426.00	37.00	80.00	37.00	80.00	33.00	33.00	33.00

Table 12
Fracture energies of the pultruded GFRP for the three-point bending beam.

G_{ft} [MPa·mm]	G_{fc} [MPa·mm]	G_{mt} [MPa·mm]	G_{mc} [MPa·mm]	G_{it} [MPa·mm]	G_{ic} [MPa·mm]
130.00	130.00	3.84	3.84	3.84	3.84

Table 13
FEM and cross-section discretizations for five different analysis cases for the three-point bending beam.

	FEM discretization	Cross-section discretization (A-A)
Case A	7 B4	150 L9
Case B	6 B4+1 B3	64 L9
Case C	6 B4+1 B2	32 L9
Case D	6 B4+1 B2	24 L9
Case E	6 B4+1 B2	16 L9

1. By analyzing Fig. 19, it is clear that the implementation of the Hashin damage model within the CUF framework manages to produce results in a better agreement with the experiments compared to the user-subroutine UMAT in Abaqus. CUF and 3D Abaqus correctly predict the pre-peak branch of the force-CMOD plot, while only CUF appears capable of foreseeing the softening. Moreover, the same consideration of the previous case can be drawn on the differences between CUF and 3D Abaqus results.
2. The use of the CUF allows a significant reduction of computational cost since its number of DOF is considerably lower than Abaqus, as reported in Table 14. Moreover, reference CUF maximum reaction is 3.5% less than the mean experimental peak, while CUF CMOD at peak results 2.2% bigger than mean reference [46].

Table 14
Comparison of CUF maximum reaction and CMOD with experimental and 3D Abaqus results, and total DOF of each model for the three-point bending beam.

Case	Total DOF	Peak load [kN]	CMOD at peak [mm]
Reference solutions			
Exp 1 — Liu et al. [46]	–	3.800	0.474
Exp 2 — Liu et al. [46]	–	4.040	0.556
Exp 3 — Liu et al. [46]	–	4.030	0.498
Exp 4 — Liu et al. [46]	–	3.530	0.458
3D Abaqus — Arruda et al. [24]	381270	3.971	0.623
Present 1D CUF models			
1D CUF Case A	36735	3.605	0.500
1D CUF Case B	15504	3.544	0.504
1D CUF Case C	7803	3.567	0.503
1D CUF Case D	6069	3.472	0.511
1D CUF Case E	4335	3.348	0.455

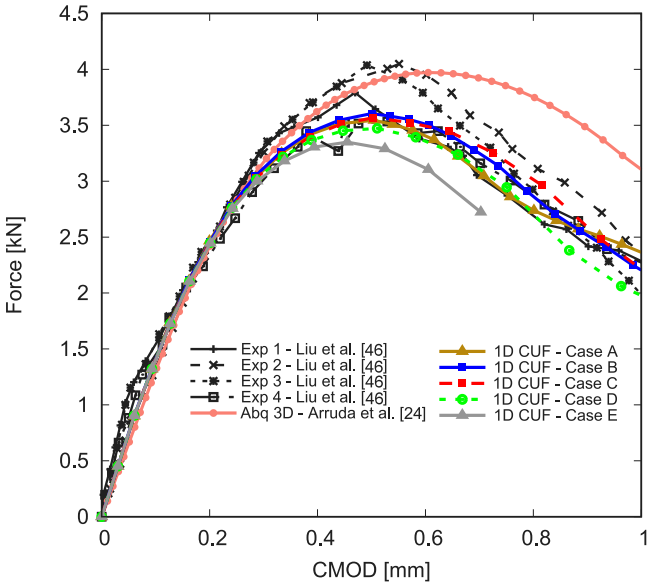

Fig. 19. Vertical load–CMOD for the three-point bending beam.

3. Fig. 21 clearly illustrates the involvement of fiber, matrix, and interlaminar damages. In addition, the current model captures some 3D effects that previous 2D models fail to appreciate [17].

5. Discussion

The first numerical result concerns the verification of the full 3D Hashin damage model within the CUF formulation. Peaks and softening match the reference CODAM2 results, precedently obtained via [29] and LS-DYNA [40]. Assessments included a single element under uniaxial longitudinal and transversal load — see Figs. 5 and 6 — and a quasi-isotropic composite, see Fig. 7. An excellent agreement was found in the damage evolution with the CODAM2 benchmark for a quasi-isotropic laminate, as shown in Fig. 8.

The second numerical assessment considers a CT coupon. A preliminary convergence study allows for the correct selection of the numerical model, namely, a single 4-node beam element along the y-direction and 157 biquadratic L9 expansions for the cross-section. The CUF results are compared to experimental [43] and 3D Abaqus benchmarks [24]. The CUF peak load is 1.8% higher than the experimental peak and significantly more accurate than the Abaqus benchmark, as shown in Table 7. Furthermore, the softening path results closer to the experimental behavior of the coupon compared to [24], as highlighted in Fig. 10. The most relevant advantage of using CUF is related to the number of DOF required for the simulation. The reference Abaqus model employs 66900 DOF, using 8-node brick solid elements for half structure; with CUF, a considerable reduction of DOF is possible since only 8950 DOF can be used for the whole model without symmetry boundary conditions, corresponding to an 87% reduction. The CUF framework can correctly simulate the pattern of damage, especially the evolution in the matrix, according to [17].

As briefly discussed in Section 4.2, mesh sensitivity is a relevant problem when dealing with continuum damage mechanics. According to the 1D CUF formulation, two types of sensitivity analyses are conducted: (i) the order of FEM elements acting along the y-direction; (ii) the order of the structural theory used for the cross-section discretization. The sensitivity analysis is outlined for different cross-sectional kinematics fields in the narrow section — see Fig. 14 — where the damage propagation occurs. Using both L4 and L9 expansions, the sensitivity analysis shows that slight differences can be detected in the peak prediction for each mesh size. The histogram bars related to the smallest size of the cross-sectional narrow band elements — see Fig. 15(b) — highlight the mesh insensitivity when using quadratic or cubic expansion orders. By employing B2 and B3 elements and L4 and L9 theories, a decrease in the size of the narrow section elements leads to a significantly lower structural theory sensitivity. The use of a B4, along with L9 elements, leads to a reduction of the mesh-size dependency, as highlighted in Fig. 16, with a percentage variation of 1.9%; mesh-size dependency with B2 and B3 is higher, respectively 2.9% and 2.2%.

The last assessment is a TPB beam with a notch at the midspan. As previously done in [24], only a quarter of the beam is considered. CUF peak load results are 3.5% lower than the average experimental peak. Still, the improvement compared to the 3D Abaqus formulation is found in the post-peak path, where the results are enclosed between the experimental curves [46]. The computational saving is evident from Table 14, since the CUF reference model, namely Case C — see Table 13 — only involves 2% of DOF required for the Abaqus model [24]. The damage evolution is consistent with the experimental pattern of damage; the matrix damage is the main involved, as shown in Fig. 20, and minor fiber damage propagation is shown in Fig. 21.

6. Conclusions

In this work, a novel orthotropic full 3D damage model is combined with one-dimensional (1D) refined finite elements (FE) based on Carrera Unified Formulation (CUF) for progressive failure analysis in composite laminates. The proven capabilities of CUF formulation are exploited here to reduce computational demand while obtaining a 3D-like solution with great accuracy. The damage model is based on the Hashin failure criterion, which is here modified to consider a full 3D stress state. This method has been first verified on a single element, which presents various stacking sequences and is subjected to different boundary conditions. Results agree with the reference solutions obtained through the CODAM2 damage model. Then, the present

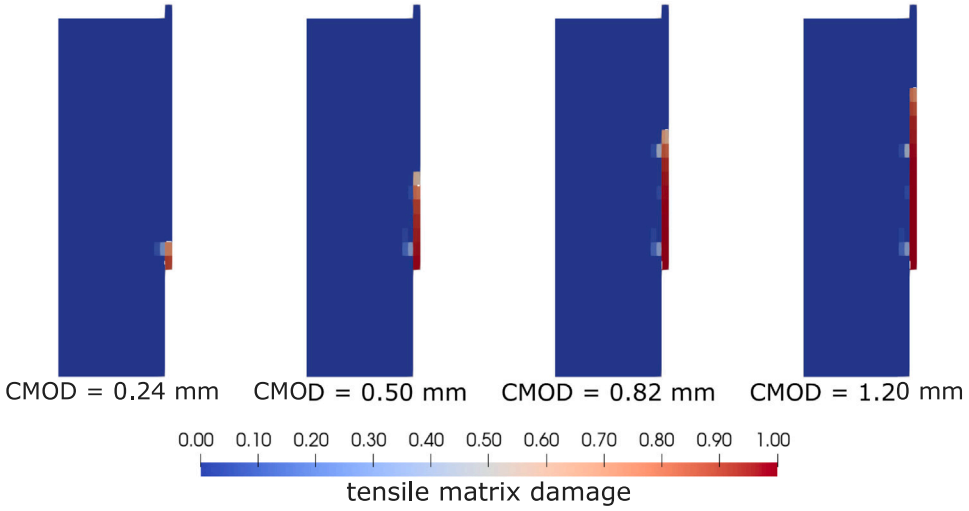

Fig. 20. Evolution of tensile matrix damage in the notch for case C of the three-point bending beam.

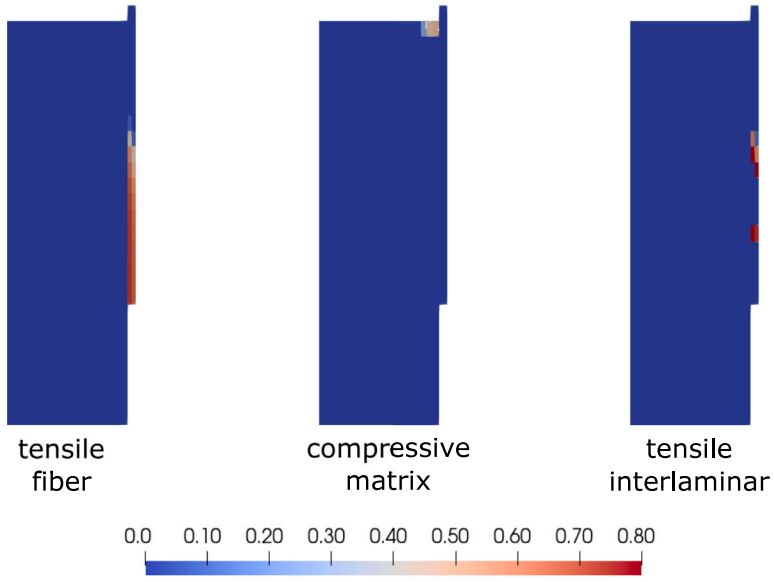

Fig. 21. Final distribution of tensile fiber, compressive matrix and tensile interlaminar damage for case C of the three-point bending beam.

method is tested on a compact tension test and a three-point bending beam. The stress–strain curves are compared with those retrieved by experimental tests and the one obtained by applying the same Hashin-based failure criteria in Abaqus, where lower-order structural theories are adopted. The results suggest that CUF can predict more accurately the softening behavior obtained through the experimental campaign if compared with the 3D Abaqus solution. The error in predicting failure load and corresponding displacement is minimal. Furthermore, the proposed method can correctly reproduce the damage distribution in the structure, including some 3D effects that two-dimensional models did not capture. These results have been obtained with a significant reduction in the computational cost of the analysis.

Future developments aim to refine the modeling of shear damage, including the nonlinearity. Moreover, future works will focus on exploiting the proposed framework for problems where the interlaminar damage mode occurs with more prominence compared to the fiber and matrix modes. The proposed methodology will be applied to implement a 3D Tsai–Wu-based model within the CUF framework and to detect and predict progressive failure in micromechanics problems.

Declaration of competing interest

The authors declare that they have no known competing financial interests or personal relationships that could have appeared to influence the work reported in this paper.

Data availability

Data will be made available on request.

Acknowledgments

This project has received funding from the European Research Council (ERC) under the European Union's Horizon 2020 research

and innovation programme (Grant agreement No. 850437). E.C. and M.E. would like to acknowledge the DEVISU project, supported by the Ministero dell'Istruzione, dell'Universitá della Ricerca research funding programme PRIN 2017, Italy (2017ZX9X4K). M.R.T.A. would also like to acknowledge Fundação para a Ciência e Tecnologia (FCT), Portugal under the Transitional Standard—DL57/2016/N3/UI/CERIS/CT/165/2018.

References

[1] Tsai SW, Wu EM. A general theory of strength for anisotropic materials. J Compos Mater 1971;5(1):58–80.
[2] Hashin Z. Failure criteria for unidirectional fiber composites. J Appl Mech 1980;47(2):329–34.
[3] Puck A, Schürmann H. Failure analysis of FRP laminates by means of physically based phenomenological models. Compos Sci Technol 2002;62(12–13):1633–62.
[4] Puck A, Schürmann H. Failure analysis of FRP laminates by means of physically based phenomenological models. In: Failure criteria in fibre-reinforced-polymer composites. Elsevier; 2004, p. 832–76.
[5] de Moura MFSF, Gonçalves JPM. Modelling the interaction between matrix cracking and delamination in carbon–epoxy laminates under low velocity impact. Compos Sci Technol 2004;64(7):1021–7.
[6] Hallett SR, Jiang W, Khan B, Wisnom MR. Modelling the interaction between matrix cracks and delamination damage in scaled quasi-isotropic specimens. Compos Sci Technol 2008;68(1):80–9.
[7] Sun XC, Wisnom MR, Hallett SR. Interaction of inter- and intralaminar damage in scaled quasi-static indentation tests: Part 2 – numerical simulation. Compos Struct 2016;136:727–42.
[8] Reiner J, Veidt M, Dargusch M, Gross L. A progressive analysis of matrix cracking-induced delamination in composite laminates using an advanced phantom node method. J Compos Mater 2017;51(20):2933–47.
[9] Wang HW, Zhou HW, Ji HW, Zhang XC. Application of extended finite element method in damage progress simulation of fiber reinforced composites. Mater Des 2014;55:191–6.
[10] Chaboche JL. Continuum damage mechanics: Part I—General concepts. J Appl Mech 1988;55(1):59–64.
[11] Tan SC, Nuismer RJ. A theory for progressive matrix cracking in composite laminates. J Compos Mater 1989;23(10):1029–47.
[12] Tan SC. A progressive failure model for composite laminates containing openings. J Compos Mater 1991;25(5):556–77.
[13] Tan SC, Perez J. Progressive failure of laminated composites with a hole under compressive loading. J Reinf Plast Compos 1993;12(10):1043–57.
[14] Apalak ZG, Apalak MK, Genc MS. Progressive damage modeling of an adhesively bonded unidirectional composite single-lap joint in tension at the mesoscale level. J Thermoplast Compos Mater 2006;19(6):671–702.
[15] Basu S, Waas AM, Ambur DR. Prediction of progressive failure in multidirectional composite laminated panels. Int J Solids Struct 2007;44(9):2648–76.
[16] Okabe T, Onodera S, Kumagai Y, Nagumo Y. Continuum damage mechanics modeling of composite laminates including transverse cracks. Int J Damage Mech 2018;27(6):877–95.
[17] Arruda MRT, Almeida-Fernandes L, Castro L, Correia JR. Tsai–Wu based orthotropic damage model. Composites C 2021;4:100122.
[18] Robbins DH, Reddy JN, Rostam-Abadi F. Layerwise modeling of progressive damage in fiber-reinforced composite laminates. Int J Mech Mater Design 2005;2:165–82.
[19] Camanho PP, Matthews FL. A progressive damage model for mechanically fastened joints in composite laminates. J Compos Mater 1999;33(24):2248–80.
[20] Warren KC, Lopez-Anido RA, Vel SS, Bayraktar HH. Progressive failure analysis of three-dimensional woven carbon composites in single-bolt, double-shear bearing. Composites B 2016;84:266–76.
[21] Matzenmiller ALJTR, Lubliner J, Taylor RL. A constitutive model for anisotropic damage in fiber-composites. Mech Mater 1995;20(2):125–52.
[22] Hühne C, Zerbst AK, Kuhlmann G, Steenbock C, Rolfes R. Progressive damage analysis of composite bolted joints with liquid shim layers using constant and continuous degradation models. Compos Struct 2010;92(2):189–200.
[23] Mandal B, Chakrabarti A. Simulating progressive damage of notched composite laminates with various lamination schemes. Int J Appl Mech Eng 2017;22(2).
[24] Arruda MRT, Trombini M, Pagani A. Implicit to explicit algorithm for ABAQUS standard user-subroutine UMAT for a 3D hashin-based orthotropic damage model. Appl Sci 2023;13(2).
[25] Geers MGD, Brekelmans WAM, De Borst R. Viscous regularization of strain-localisation for damaging materials: Viscous and rate-dependent constitutive models. In: DIANA computational mechanics '94: Proceedings of the first international diana conference on computational mechanics. Springer; 1994, p. 127–38.
[26] Carrera E, Cinefra M, Petrolo M, Zappino E. Finite element analysis of structures through unified formulation. John Wiley & Sons; 2014.
[27] Carrera E, Pagani A, Petrolo M. Component-wise method applied to vibration of wing structures. J Appl Mech 2013;80(4).
[28] Shen J, Arruda MRT, Pagani A. Concrete damage analysis based on higher-order beam theories using fracture energy regularization. Mech Adv Mater Struct 2022;1–15.
[29] Nagaraj MH, Reiner J, Vaziri R, Carrera E, Petrolo M. Progressive damage analysis of composite structures using higher-order layer-wise elements. Composites B 2020;190:107921.
[30] Nagaraj MH, Reiner J, Vaziri R, Carrera E, Petrolo M. Compressive damage modeling of fiber-reinforced composite laminates using 2D higher-order layer-wise models. Composites B 2021;215:108753.
[31] Williams KV, Vaziri R, Poursartip A. A physically based continuum damage mechanics model for thin laminated composite structures. Int J Solids Struct 2003;40(9):2267–300.
[32] Forghani A, Poursartip A, Vaziri R. An orthotropic non-local approach to modeling intra-laminar damage progression in laminated composites. Int J Solids Struct 2019;180–181:160–75.
[33] Carrera E, Petrolo M. Refined beam elements with only displacement variables and plate/shell capabilities. Meccanica 2012;47(3):537–56.
[34] Bathe K-J. Finite element procedures. 2006.
[35] Lemaitre J, Benallal A, Billardon R, Marquis D. Thermodynamics and phenomenology. 2002, p. 209–23.
[36] Lemaitre J, Chaboche JL. Mechanics of solid materials. Cambridge University Press; 1994.
[37] Lapczyk I, Hurtado JA. Progressive damage modeling in fiber-reinforced materials. Composites A 2007;38(11):2333–41.
[38] Bazant Z, Oh B. Crack band theory for fracture of concrete. Mater. Constr. 1983;16:155–77.
[39] Shen J, Arruda MRT, Pagani A, Carrera E. A regularized higher-order beam elements for damage analysis of reinforced concrete beams. Mech Adv Mater Struct 2023.
[40] Reiner J, Feser T, Schueler D, Waimer M, Vaziri R. Comparison of two progressive damage models for studying the notched behavior of composite laminates under tension. Compos Struct 2019;207:385–96.
[41] Almeida-Fernandes L, Silvestre N, Correia JR. Characterization of transverse fracture properties of pultruded GFRP material in tension. Composites B 2019;175:107095.
[42] Girão Coelho AM, Toby Mottram J, Harries KA. Finite element guidelines for simulation of fibre-tension dominated failures in composite materials validated by case studies. Compos Struct 2015;126:299–313.
[43] Almeida-Fernandes L, Silvestre N, Correia JR, Arruda MRT. Fracture toughness-based models for damage simulation of pultruded GFRP materials. Composites B 2020;186:107818.
[44] Hughes TJR. The finite element method: Linear static and dynamic finite element analysis. Courier Corporation; 2012.
[45] Lopes B, Arruda MRT, Almeida-Fernandes L, Castro L, Silvestre N, Correia JR. Assessment of mesh dependency in the numerical simulation of compact tension tests for orthotropic materials. Composites C 2020;1:100006.
[46] Liu W, Feng P, Huang J. Bilinear softening model and double k fracture criterion for quasi-brittle fracture of pultruded FRP composites. Compos Struct 2017;160:1119–25.